Granule-by-granule reconstruction of a sandpile from x-ray microtomography data

G. T. Seidler,[1,2,*] G. Martinez,[1] L. H. Seeley,[1] K. H. Kim,[1] E. A. Behne,[1] S. Zaranek,[1] B. D. Chapman,[1] S. M. Heald,[2,3] and D. L. Brewe[1,2]

[1]*Physics Department, University of Washington, Seattle, Washington 98195-1560*

[2]*PNC-CAT Sector 20, Advanced Photon Source, Argonne, Illinois 60439*

[3]*Pacific Northwest National Labs, Richland, Washington 99352*

(Received 25 April 2000)

Mesoscale disordered materials are ubiquitous in industry and in the environment. Any fundamental understanding of the transport and mechanical properties of such materials must follow from a thorough understanding of their structure. However, in the overwhelming majority of cases, experimental characterization of such materials has been limited to first- and second-order structural correlation functions, i.e., the mean filling fraction and the structural autocorrelation function. We report here the successful combination of synchrotron x-ray microtomography and image processing to determine the full three-dimensional real-space structure of a model disordered material, a granular bed of relatively monodisperse glass spheres. Specifically, we determine the center location and the local connectivity of each granule. This complete knowledge of structure can be used to calculate otherwise inaccessible high-order correlation functions. We analyze nematic order parameters for contact bonds to characterize the geometric anisotropy or fabric induced by the sample boundary conditions. Away from the boundaries we find short-range bond orientational order exhibiting characteristics of the underlying polytetrahedral structure.

PACS number(s): 45.70.Qj, 07.85.Qe, 46.65.+g

I. INTRODUCTION

The granular bed, or colloquially the sandpile, has become one of the condensed matter physicist's favorite model systems [1], encompassing geometric frustration [2], nonlinear response [3], and self-organization [4]. In addition to conceptual appeal, the simplest granular beds consisting of monodisperse hard spheres have relevance for several physical systems, including powders [5], liquids [6], and metallic glasses [7,8]. Direct measurement of the structure of random dense packings of hard spheres by mechanical disassembly has been reported by Bernal [6,9], Scott [10], and Finney [11]. Although the ''reference structures'' obtained in their work have proven to be important, the tedious granule-by-granule disassembly that they employed has discouraged imitation; reference structures exist for only a few packing fractions of extremely monodisperse spheres with small intergranule friction. The absence of a more varied database of reference structures is particularly unfortunate in view of both the theoretical interest [2,12–17] in bond orientational order in three-dimensional (3D) dense random packings and also the extensive work on effective transport properties of hard-sphere systems [18]. Although magnetic resonance imaging (MRI) has proven useful in 3D imaging of representative sections of granular flow [19], MRI is too time intensive for the complete 3D imaging of structure. Conversely, scanning confocal microscopy has been used to determine the 3D structure of specially prepared colloidal glasses [20], but is not generally applicable to dry granular media.

Here, we report the successful granule-by-granule virtual reconstruction of a sandpile from three-dimensional synchrotron x-ray microtomography (XMT) data. Our technique is both rapid and noninvasive, allowing one to study iterative changes on application of an external perturbation, and can be used on systems large enough to avoid contamination of the bulk disordered structure by boundary effects. Synchrotron XMT has previously been used to determine some high-order mass distribution functions of sandstone [21] and of a magnetic gel [22] as a means to testing effective transport theories. The technique presented here additionally allows the measurement of high-order *n*-sphere correlation functions, from which many other physically relevant correlation functions (including the *n*-point mass functions [23]) can be calculated.

Below, we present details of our tomography apparatus and data collection, then describe the use of 3D image processing to identify the central position and local connectivity of more than 2000 granules in our test sample. Our results for the radial distribution function of sphere centers and for the distribution of physical coordination number agree well with the previous results obtained by mechanical disassembly. We then use nematic order parameters to investigate possible bond orientational order. In the central, geometrically isotropic region of the test sample, we find short-range bond orientational order with a symmetry more complicated than but related to nematic symmetry. Before concluding, we discuss the possible application of our technique to samples with as many as 10^5 granules.

II. EXPERIMENT

All measurements were performed at sector 20-ID of the Pacific Northwest Consortium Collaborative Access Team (PNC-CAT) beamlines at the Advanced Photon Source x-ray synchrotron located at Argonne National Labs. The area detector of our prototype tomography apparatus follows the

*Author to whom correspondence should be addressed. Email address: seidler@phys.washington.edu

general considerations of Koch *et al.* [24], with the exception that an inexpensive eight-bit room temperature charge-coupled-device (CCD) camera (EDC-1000 U, Electrim) was used as a cost-saving measure during instrument development. One rectangular CCD pixel corresponds to a radiogram subregion with lateral scale 3.5 μm and vertical scale 6.2 μm. The tomography sample stage consists of two miniature linear translators for centering mounted on a motorized rotary stage (ART-50, Aerotech). The rotary stage is itself mounted on a two-axis motorized tilt stage; these two degrees of freedom are used to ensure that the rotation axis is simultaneously perpendicular to the beam direction and to the effective CCD line scan direction with a precision of 10^{-5} rad in each angle.

Our test sample is a simple granular bed consisting of mean diameter $D=63$ μm glass spheres (>95% have polydispersivity ± 4 μm, MOSCI, USA) in a vertical 1.0 mm inner-diameter glass cylinder. We will use $R_c=0.5$ mm to denote the radius of the cylinder. Spheres were slowly poured into the cylinder through a paper funnel; room humidity was sufficiently low that no clumping was apparent during pouring. The sample was then vertically agitated by an electromagnetic shaker for 1000 cycles with a maximum acceleration of 22.5 m/s^2, resulting in a 2-cm tall region of densely packed spheres. As is discussed in Sec. IV, the mean packing fraction of the sample is $\sim$0.61. Next, the granular bed was mounted onto the tomography sample stage with the cylinder axis along the apparatus rotation axis, and the necessary rotational sequence of 560 radiographs was collected at a photon energy of 20 keV for the same sample volume for sample-to-detector distances of 2, 8, 14, and 20 cm. Each one of these data sets provided completely satisfactory tomograms; the different distances were chosen to investigate the phase contrast effects discussed in Sec. III, below. The region studied had a height of 630 μm and was located at approximately midheight of the test sample. The low capacity of our camera was satisfactorily compensated by integrating 10 exposures, although this resulted in a total measurement time of $\sim$90 min. A standard filtered backprojection algorithm [25] is used to reconstruct the tomographs from the rotational sequence of radiograms after corrections for beam structure and detector dark count. Both data collection and tomograph processing (with a Fortran DLL) are performed in LabView; all other computation described below is performed in the IDL programming environment. We show typical cuts through the three-dimensional tomograph in Figs. 1(a) and 1(b).

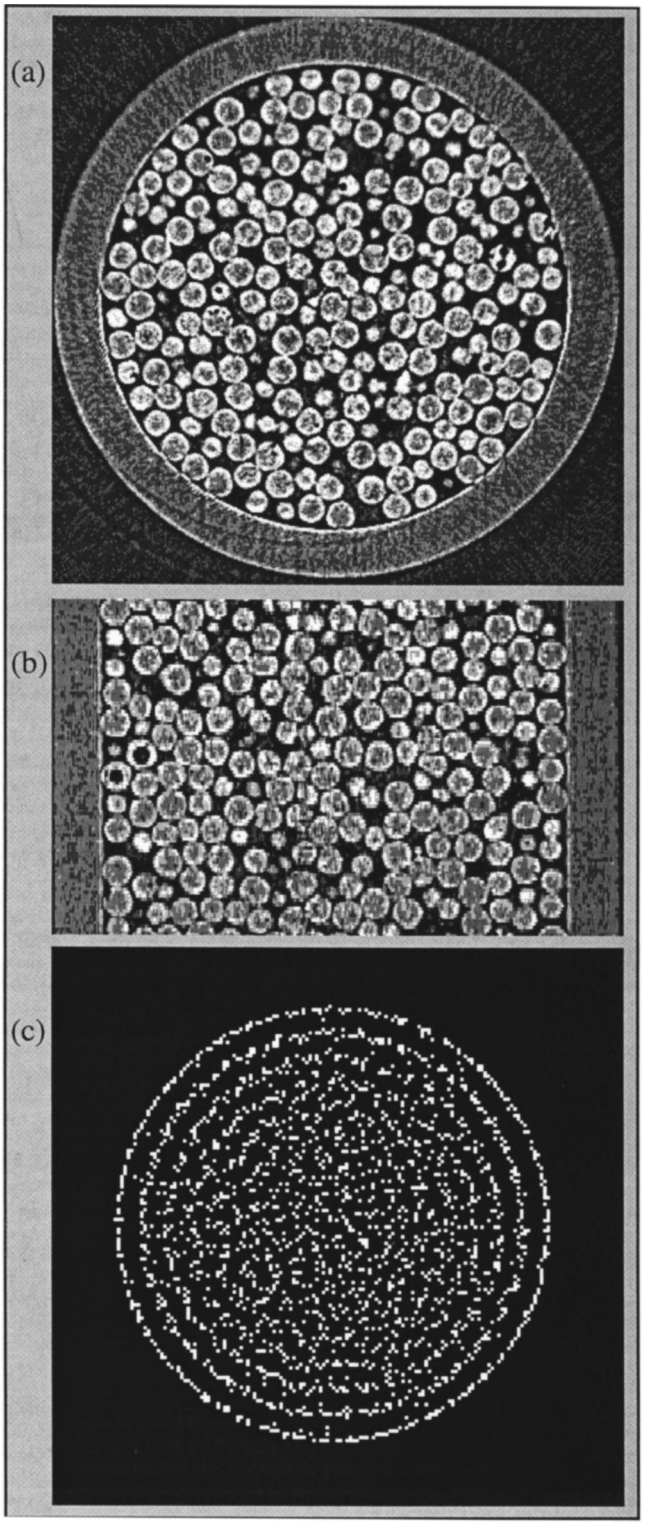

FIG. 1. Two perpendicular cuts through the full 3D tomograph of a granular bed consisting of mean diameter $D=63$ μm spherical glass beads in a 1.0-mm inner-diameter glass cylinder. (a) A cut perpendicular to the cylinder axis. (b) A cut parallel to the *xz* plane. (c) A projection down the cylinder axis of the granule centers as determined by the 3D Hough transform. See the text for details.

III. ALGORITHMS FOR SPHERE RECOGNITION

The first step in object recognition is edge location. To optimize edge location, we intentionally configure the experiment to take advantage of x-ray phase effects. Studies of the geometric optics of x-rays date to the earliest attempts to determine the nature of x radiation [26]. The development of highly collimated and sometimes highly coherent x-ray beams at the third generation x-ray synchrotrons has led to a recent renewal of interest in x-ray phase contrast phenomenon [27–29]. As the dielectric constant of all materials in the x-ray range is less than unity, spherical bodies act as (admittedly weak) diverging lenses for x rays. Additionally, the near-tangential incidence to the surface of a sphere can result in total external reflection.

Phase effects occur here as concentric circular halo artifacts of enhanced absorption inside enhanced source sur-

rounding the shadow of a spherical grain in any radiograph. The halo features in the original radiographs result in corresponding concentric shells of anomalous absorption and source surrounding each granule in the final reconstructed 3D tomograph. Normally, one would avoid these artifacts by putting the detector close enough to the sample to ensure that refracted or externally reflected intensity would deviate laterally by less than a pixel at the detector. However, these artifacts provide a beneficial edge contrast enhancement at no cost in noise. Phase contrast artifacts in the 3D tomograph of our test sample result in improved performance by 3D Sobel gradient edge location [30]. The enhancement of the Sobel numerical gradient was optimal for the 14 cm sample-to-detector separation; all results reported here are calculated from that data set. Voxels with a magnitude of the numerical gradient vector above a threshold value are identified as candidate edge voxels.

The second and final step in our object recognition software is a Hough sphere transform [31]. Although the Hough transform was originally proposed as an automation tool for specific patterns occurring in bubble chambers in high-energy physics experiments [32], it has subsequently been generalized to become a canonical tool of computer vision [33]. The reduced Hough sphere transform used here maps the location and numerical gradient vector of candidate edge voxels onto the space of center coordinates using the dispersion of sphere radii as a known parameter. The centroid of a cluster of high intensity in the space of center coordinates is taken as the center of a granule. The void inclusions present in some granules [see Figs. 1(a) and 1(b)] do not affect these results because the gradient vectors at the inclusion-to-glass boundaries are directed outward. The range space of the full Hough transform is the product space of center positions and sphere radii, meaning that future studies on strongly polydisperse samples may use the full transform to more reliably determine the local connectivity of each granule.

IV. RESULTS AND DISCUSSION

In Fig. 1(c) we show a projection down the cylinder axis of the 2210 granule centers identified by the Hough transform. The most effective test to verify that all granule centers have been found is a void space test. In this test one determines if there exists a void sufficiently large to insert one more granule into the virtual system consisting of granules of the mean diameter placed at the candidate center locations. In the present case, exactly one such void is present in the virtual sample, but is in fact the real location of one ellipsoidal granule with a very large major axis (~ 90 μm). This single granule does not affect the results presented here. We have verified the complete accuracy of our granule identification with several additional tests, including section-by-section comparison of the experimentally determined 3D tomograph with a simulated 3D tomograph based on the candidate center locations. Based on the sample volume, the number of granules, and the mean granule diameter, we find a mean packing fraction of 0.61 ± 0.01.

In Fig. 2 we show the normalized cylindrical density function for granule centers in the test sample. Note that ρ is the distance from the center of the cylinder while β is the distance from the container wall in units of the mean granule diameter D. The strong boundary effect decays fully after five bands spaced by $\Delta\beta = 0.82 \pm 0.01$, consistent with the tetrahedral height $\tau = 0.8165$ that is expected for the close packing of hexagonal sheets.

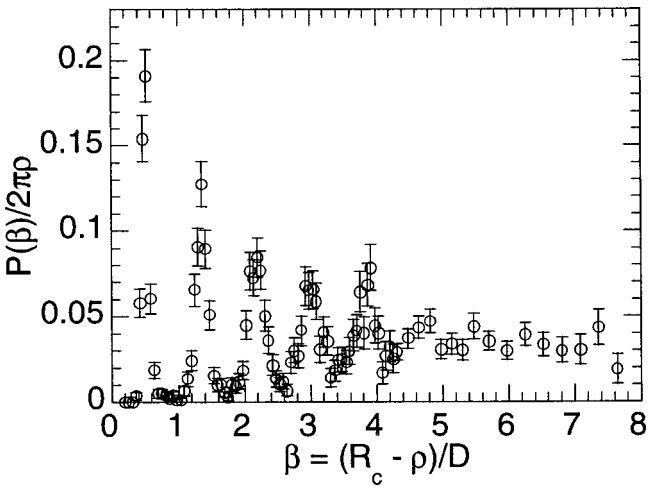

FIG. 2. The normalized cylindrical density function for sphere centers as a function of distance β from the cylinder wall in units of the mean granule diameter D.

In much of the remainder of this paper, we discuss a standard methodology for characterizing bond orientational order, including order that may be induced by the cylindrical symmetry of the boundary conditions. For this purpose, it is useful to define the set **G** of 359 granules whose centers are at least $4.5D$ away from the wall of the cylinder. Note that the one strongly ellipsoidal granule discussed above is located outside of **G**.

We show in the main part of Fig. 3 the radial distribution function for granules in **G** as a function of the reduced sepa-

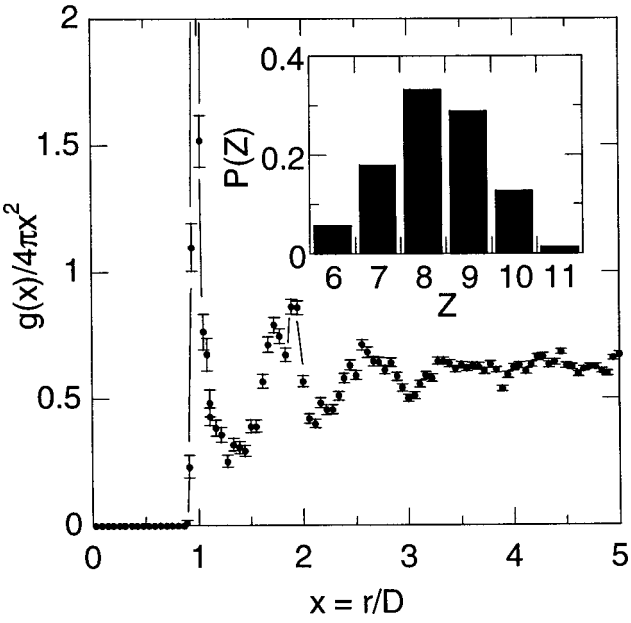

FIG. 3. The normalized radial distribution function for sphere centers in the cylindrical subsample **G** defined in the text. Solid lines are guides to the eye. Inset: The probability distribution function for coordination number Z of granules in **G** as defined by a contact criterion. This distribution has $\langle Z \rangle = 8.3$.

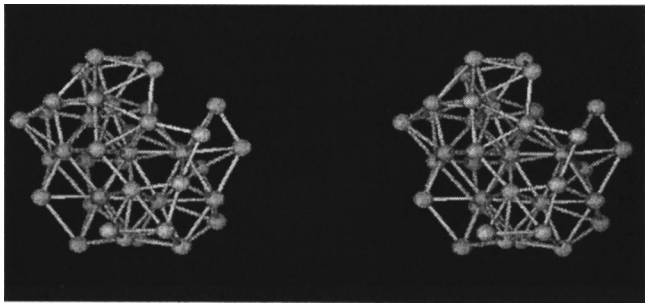

FIG. 4. A steropair showing the computed bond network for a small cluster in the random packing. The small spheres indicate the locations of granule centers and the edges indicate contact between the corresponding granules. Note the region of partial icosahedral ordering in the upper left corner of the cluster.

ration $x=r/D$. Allowing for the weak polydispersivity of our sample, the results are in good agreement with previous experiments [11] and simulations [15] on random dense packings. The width of the peak at $x=1$ is consistent with the polydispersivity of our granules, and is considerably less than the convolution of the polydispersivity with the resolution of a single pixel on our detector. This important experimental detail is a consequence of the subpixel performance of Hough transforms with large numbers of edge projections [33]. In the present case, each of more than 200 edge voxels per granule provide an estimate of the center position with an accuracy of two to three voxel spacings. Gaussian statistics then imply a final error in the center coordinates of ~ 0.2 pixel spacings or $\sim 0.01D$.

The high-precision data for granule centers can be used to calculate a wide variety of physically relevant high-order correlation functions [34]. Here, we continue our computations to determine local connectivity and correlation functions relevant for bond orientational order. Connectivity of sphere packings can be discussed in two contexts. In one case connectivity refers to physical contact between densely packed granules, while in the second case connectivity is determined by a Wigner-Seitz construction [35] wherein grains are termed nearest neighbors when they influence each other's Wigner-Seitz cells (Voronoi polyhedra), irrespective of physical contact. Here, we focus on the former context, where granules are termed nearest neighbors if and only if they have physical contact; an analysis of bond orientational order as it relates to local symmetry in the Sietz context will be presented elsewhere [34].

We use the simplest contact criterion consistent with the granule polydispersivity to specify coordination, i.e., that the separation distance between centers be less than $1.06D$. Based on the measured $g(r)$ in Fig. 3, this will produce less than 3% total missed or spurious bonds. We show in the inset to Fig. 3 the probability density function $P(Z)$ for coordination number Z of granules which are in **G** and also at least $1.5D$ away from the top and bottom surfaces of the data set. Granules immediately outside of **G** but in contact with granules at the boundary of **G** are included when counting contacts. Both $\langle Z\rangle = 8.3$ and the form of $P(Z)$ are in good agreement with the ball-bearing reference structures [9,11] and with more recent simulation [15]. We present in Fig. 4 a stereoprojection pair depicting a small subsection of the computed 3D contact bond network of our sample.

Considerable evidence exists that interparticle forces overwhelm individual granule weights when deep in the interior of a relaxed or compacted granular bed [1,36]. Therefore structural ansiotropy induced by the boundary conditions [37] of the sample is expected to be more important than anisotropy induced by gravity. Here, we will directly characterize anisotropy using nematic order parameters [38] of the form $Q_{\hat{n}}=\frac{1}{2}[3\cos^2(\phi_{\hat{n}})-1]$, where $\hat{n}$ is the Frank director and $\phi_{\hat{n}}$ is the angle between the bond and the director. Note that $Q_{\hat{n}}$ is equal to unity when the system is completely ordered with every bond parallel to $\hat{n}$, is equal to zero for randomly oriented bonds, and is equal to $-\frac{1}{2}$ when every bond is directed perpendicular to $\hat{n}$. Isotropy would require that contact bond directions with respect to any $\hat{n}$ be uniformly distributed on the surface of the half sphere with the probability density $P(\phi_{\hat{n}})=\sin(\phi_{\hat{n}})$. Changing variables from $\phi_{\hat{n}}$ to $Q_{\hat{n}}$,

$$P(Q_{\hat{n}}) = 1/\sqrt{6Q_{\hat{n}}+3}. \tag{1}$$

Given the cylindrical symmetry of the sample container, the two relevant directors are $\hat{n}=\hat{z}$ (vertical) and $\hat{n}=\hat{\rho}$ (cylindrical radial).

We show in Fig. 5 the probability density functions for $Q_{\hat{z}}$ (open circles) and $Q_{\hat{\rho}}$ (filled triangles) for bonds whose centers are contained in **G** (top figure) or outside of **G** (bottom figure). Errors are calculated from binomial statistics. In both the top and bottom parts of the figure, the solid line indicates the prediction of Eq. (1) when smoothed by the bin size in the measured density functions. Comparison of the prediction for isotropy with the measured $P(Q_{\hat{z}})$ and $P(Q_{\hat{\rho}})$ for bonds in **G** yields reduced chi-squared of $\chi^2_v=1.2$ and $\chi^2_v=0.9$ for $v=19$ degrees of freedom, respectively. Note that $\langle Q_{\hat{z}}\rangle = -0.003\pm 0.012$ and $\langle Q_{\hat{\rho}}\rangle = 0.006\pm 0.012$, again consistent with isotropy. The residuals between the experimental distributions and the prediction for isotropy (top inset) are randomly distributed. Hence, to the limits imposed by small sample statistics, the central subsample **G** is isotropic. Conversely, the region of the sample outside G [which includes the packing bands evident in Fig. 1(c) and Fig. 2] has the expected strong anisotropy with the large value of $P(Q_{\hat{\rho}}=-0.5)$ indicating a preference for bond orientations perpendicular to $\hat{\rho}$, i.e., parallel to the bands. The anisotropy with respect to $\hat{z}$ are much weaker but still statistically significant ($\chi^2_v=8.2$ for $v=19$). The largest residual from isotropy is for $Q_{\hat{z}}=1$, where the positive residual indicates a tendency for granules to align in vertical chains in the outermost layer of granules.

Although the bond directions in **G** are isotropic on average, one may still ask if short-range bond orientational order exists. Such correlations have been addressed by theory [2,12–13] and simulation [14–17] and have been calculated for simulationally relaxed reference structures [2]. Here, we continue with the theme of using only the simplest order parameter consistent with the symmetry of a bond. We define the vector order parameter $Q_{2m}(\vec{\mathbf{r}})=Y_{2m}[\theta(\vec{\mathbf{r}}),\phi(\vec{\mathbf{r}})]$ for $m=-1,0,1$. The bond orientational correlation function is then

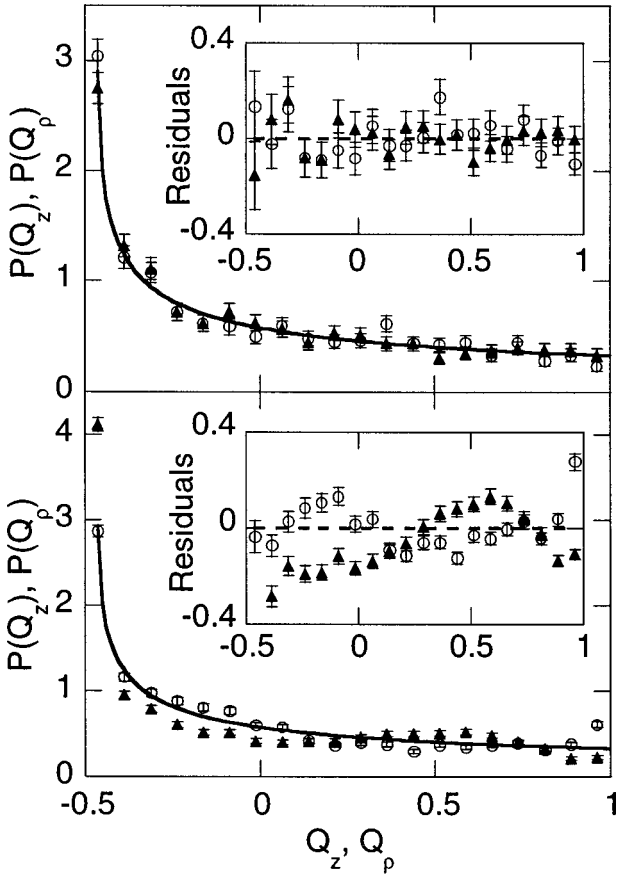

FIG. 5. The probability density functions (PDFs) for the nematic order parameters with respect to the vertical and cylindrical radial directions. The solid line shows the expected behavior for isotropic bonds with respect to the directors; see the text for details. Top: The PDFs for bonds in **G**. Bottom: The PDFs for bonds outside of **G**. Insets: The residuals between the data and the expected behavior for isotropy. Note that the extreme residual for $P(Q_{\hat{\rho}}=-0.5)$ is not included in the bottom inset.

$$Q_2(\mathbf{r}) \equiv \frac{4\pi}{5} \sum_{m=-1}^{1} \langle Q_{2\mathrm{m}}(\vec{\mathbf{r}}) Q_{2m}(0) \rangle = \langle P_2[\hat{\mathbf{n}}(\vec{\mathbf{r}}) \cdot \hat{\mathbf{n}}(0)] \rangle, \tag{2}$$

where the angled brackets indicate an average over origin and direction and where P_2 is the second Legendre polynomial. In Fig. 6 we show $Q_2(x)$ where again $x=r/D$. The small x behavior shows clear signatures of steric constraints; the strong anticorrelation at $x=-0.7$ is due to the $\pi/2$ angle between the directions of next nearest neighbor bonds (i.e. opposite edges) on a single tetrahedron, while the strong correlation close to $x=1$ is due to bonds on opposite sides of one granule or to small ordered clusters with triangular packing in a plane.

The large x behavior, where one might hope for universality between hard-sphere and soft-sphere models, shows damped oscillations with a single mode. In the inset a least-squares fit of the region $x>2.5$ to the empirical form

$$Q_2(x) = A \exp(-x/\lambda) \sin(2\pi x/L) \tag{3}$$

yields $A=0.49\pm0.12$, $\lambda=1.08\pm0.09$, and $L=0.826\pm0.003$, with $\chi_v^2=1.2$ for $v=43$. The two lengths λ and L have an additional systematic error of 1% from the uncertainty in the mean granule diameter expressed in voxel units; including all errors $\lambda=1.08\pm0.10$ and $L=0.826\pm0.011$. Note that the wavelength of the damped oscillations L is consistent with the height $\tau=0.8165$ of a unit tetrahedron. The oscillations in Fig. 6 imply that the Q_{2m} contain only part of the symmetry of the correct orientational order parameter. The situation is analogous to using magnetization to characterize a short-range ordered antiferromagnet or chiral magnet—the average magnetization vanishes but the radial autocorrelation function for the magnetization would show an exponential envelope on top of oscillations whose periods are related to the antiferromagnetic order or to the spiral pitch. The consistency between L and τ is reassuring for the present polytetrahedral system, but unfortunately does not uniquely specify the missing symmetry. We have reproduced the behavior in Fig. 6 for larger samples and will discuss several candidate order parameters elsewhere for a wider range of samples [34].

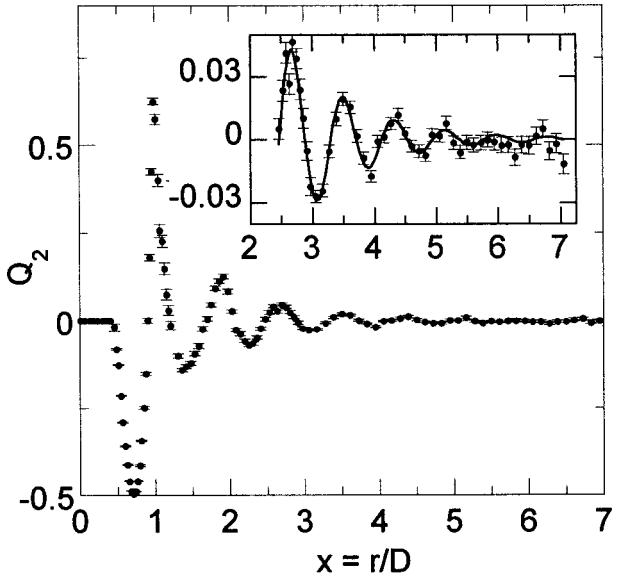

FIG. 6. The bond orientational correlation function $Q_2(x)$ for bonds contained in the subsample **G**. Inset: A least squares fit of Eq. (3) to the region $x>2.5$. See the text for details.

V. LARGER SAMPLES

Before concluding, it is important to discuss improvements to our apparatus and the feasibility of studying samples with many more granules, and specifically with a larger ratio of cylinder size to granule diameter. We will restrict our discussion to the use of insertion device (ID) beamlines at third generation x-ray synchrotrons [39]. We will also assume an that upgrade to a typical 12-bit, thermoelectrically cooled, interline transfer CCD will result in an order-of-magnitude faster data collection, giving ~10 min total data collection time for the sample studied here [40]. The discussion that follows demonstrates one set of experimental parameters that would allow measurement of samples of $\sim 10^5$ granules in a feasible measurement time; we expect that there are many combinations of experimental conditions that can satisfy this goal. We consider only absorption tomography below; however, phase tomography [28] at higher

energies might be preferable if an efficient high-spatial resolution (1-μm) high-energy phosphor were available.

To avoid the loss of x-ray flux and detector efficiency, it is preferable to remain at 20 keV and instead consider granules of different composition for the same granule diameter as in the present study. Consider granules of cellulose, fluorocarbon polymer, or nanoporous silica glass placed into a cylindrical tube with an inner diameter of 6.5 mm. This would give $\sim$100 sphere diameters across the sample but correspond to $\sim$2 absorption lengths, a convenient value for tomography measurements. The increased number of sample rotations together with the need to repeat the rotational sequence of radiographs at four sample translations (due to the 2-mm useful horizontal region of an ID x-ray beam) give a factor of 30 increase in data collection time. Two 12-bit exposures at each angle would give a contrast between granule and void in the final tomograph of at least a factor of 10 above the counting statistics, comparable to the contrast in the present study. The expected total measurement time would then be $\sim$14 h for a sample 100-granule diameters wide and 17-granule diameters high, with a total data set of $\sim$30 GB. The height of the sample is limited by the 1-mm useful vertical region of the ID x-ray beam. Such a sample would have $\sim 1.7\times 10^5$ granules for typical packing densities.

Using the same software as in the present study, the total time to invert the 3D tomogram and to perform granule location would be $\sim$200 h on a 400 MHz Pentium III processor. Note that both the tomogram inversion (in different slices) and the granule identification (in different subvolumes) are compatible with parallel processing, so that even minimal distribution on a few laboratory computers would suffice.

VI. CONCLUSIONS

We have demonstrated the automated granule-by-granule reconstruction of the three-dimensional structure and connectivity of a sandpile of monodisperse spherical granules starting from synchrotron x-ray microtomography data. We project that this technique is amenable to appropriately chosen samples with 10^5 granules. This capability enables the measurement of a broad range of otherwise unobtainable structural correlation functions for dense random packings. Nematic order parameters were used to characterize the range of boundary effects, to directly demonstrate isotropy for the interior structure of a dense random packing of hard spheres, and to reveal short-range bond orientational order. Minimal changes to the object recognition software would allow analogous studies of sandpiles of strongly polydisperse spherical granules. Sandpiles of irregularly shaped granules, such as naturally occurring soils, can be studied with the 3D synchrotron microtomography apparatus described here, but granule-by-granule reconstruction would require the development of new object recognition algorithms.

ACKNOWLEDGMENTS

We thank L. Atkins, M. den Nijs, H. Jaeger, D. Mancini, S. Nagel, D. Nelson, M. Rivers, L. Shapiro, L. Sorensen, E. Stern, D. Thouless, and E. Variano for helpful discussions. G.T.S. acknowledges support from the Alfred P. Sloan Foundation, L.H.S. acknowledges support from the Achievement Rewards for College Students program and the Leonard X. Bosack and Bette M. Kruger Charitable Foundation, and S.Z. acknowledges support from the U.S. National Science Foundation Research Experience for Undergraduates Program under Contract No. PHY-9732143. This work was supported by the Research Corporation, by the Alfred P. Sloan Foundation, and by a Junior Faculty Development Grant from the University of Washington. The operation of the PNC-CAT beamlines is supported by the U.S. Department of Energy, Basic Energy Sciences, Office of Science, under Contract No. DE-FG03-97ER45628. The operation of the Advanced Photon Source is supported by the U.S. Department of Energy, Basic Energy Sciences, Office of Science, under Contract No. W-31-109-Eng-38.

[1] H. M. Jaeger, S. R. Nagel, and R. P. Behringer, Rev. Mod. Phys. **68**, 1259 (1996).

[2] See D. R. Nelson and F. Spaepan, in *Solid State Physics*, edited by H. Ehrenreich and D. Turnbull (Academic, Boston, 1989), Vol. 42, p. 1, and references therein.

[3] A. Coniglio, Philos. Mag. B **77**, 213 (1998); R. A. Guyer, J. Ten Cate, and P. Johnson, Phys. Rev. Lett. **82**, 3280 (1999); D. L. Johnson, H. A. Makse, N. Gland, and L. Schwartz, Physica B **279**, 134 (2000).

[4] P. Bak, C. Tang, and K. Wiesenfeld, Phys. Rev. Lett. **59**, 381 (1987); A. Mehta and G. C. Barker, Rep. Prog. Phys. **57**, 383 (1994); D. L. Turcotte, *ibid.* **62**, 1377 (1999).

[5] D. J. Cumberland and R. J. Crawford, *The Packing of Particles* (Elsevier, Amsterdam, 1987).

[6] J. D. Bernal, Nature (London) **183**, 141 (1959); J. D. Bernal, Proc. R. Soc. London, Ser. A **280**, 299 (1964).

[7] See C. S. Cargill III, in *Solid State Physics*, edited by F. Seitz and D. Turnbull (Academic, New York, 1975), Vol. 30, p. 227.

[8] T. Ichikawa, Phys. Status Solidi A **19**, 707 (1973).

[9] J. D. Bernal and G. Mason, Nature (London) **188**, 910 (1960); J. D. Bernal, G. Mason, and K. R. Knight, *ibid.* **194**, 958 (1962); J. D. Bernal, I. A. Cherry, J. L. Finney, and K. R. Knight, J. Phys. E **3**, 388 (1970).

[10] G. D. Scott, Nature (London) **188**, 908 (1960); **193**, 465 (1962); G. D. Scott and D. M. Kilgour, Jr., J. Phys. D **2**, 863 (1969).

[11] J. L. Finney, Proc. R. Soc. London, Ser. A **319**, 479 (1970).

[12] H. S. M. Coxeter, Ill. J. Math. **2**, 746 (1958); H. S. M. Coxeter, *Regular Polytopes* (Dover, New Jersey, 1973); H. S. M. Coxeter, *Introduction to Geometry*, 2nd ed. (Wiley, New York, 1989); M. Kleman and J. F. Sadoc, J. Phys. (France) Lett. **40**, L569 (1979); J. F. Sadoc, J. Phys. (Paris), Colloq. **41**, C8-326 (1980).

[13] D. R. Nelson, Phys. Rev. Lett. **50**, 982 (1983); Phys. Rev. B **28**, 5515 (1983); J. Sethna, Phys. Rev. Lett. **51**, 2198 (1983); S. Sachdev and D. R. Nelson, *ibid.* **53**, 1947 (1984); J. P. Sethna, Phys. Rev. B **31**, 6278 (1985); S. Sachdev and D. R. Nelson, *ibid.* **32**, 1480 (1985).

[14] P. J. Steinhardt, D. R. Nelson, and M. Ronchetti, Phys. Rev. Lett. **47**, 1297 (1981); Phys. Rev. B **28**, 784 (1983).
[15] A. S. Clarke and H. Jonsson, Phys. Rev. E **47**, 3975 (1993).
[16] H. Jonnson and H. C. Andersen, Phys. Rev. Lett. **60**, 2295 (1988); R. M. Ernst, S. R. Nagel, and G. S. Grest, Phys. Rev. B **43**, 8070 (1991); M. D. Rintoul and S. Torquato, J. Chem. Phys. **105**, 9258 (1996).
[17] S. Torquato, T. M. Truskett, and P. G. Debenedetti, Phys. Rev. Lett. **84**, 2064 (2000).
[18] S. Torquato, Appl. Mech. Rev. **44**, 37 (1991), and references therein; J. Quintanilla, Polym. Eng. Sci. **39**, 559 (1999), and references therein.
[19] See E. Fukushima, Annu. Rev. Fluid Mech. **31**, 95 (1999), and references therein; E. E. Ehrichs, J. K. Flint, H. M. Jaeger, J. B. Knight, S. R. Nagel, G. S. Karczmar, and V. Y. Kuperman, Philos. Trans. R. Soc. London, Ser. A **356**, 2561 (1998); T. Shinbrot, A. Alexander, and F. J. Muzzio, Nature (London) **397**, 675 (1999).
[20] A. Van Blaaderen and P. Wiltzius, Science **270**, 1177 (1995); E. R. Weeks, J. C. Crocker, A. C. Levitt, A. Schofield, and D. A. Weitz, *ibid.* **287**, 627 (2000).
[21] P. Spanne, J. F. Thovert, C. J. Jacquin, W. B. Lindquist, K. W. Jones, and P. M. Adler, Phys. Rev. Lett. **73**, 2001 (1994).
[22] M. D. Rintoul, S. Torquato, C. Yeong, D. T. Keane, S. Erramilli, Y. N. Jun, D. M. Dabbs, and I. A. Aksay, Phys. Rev. E **54**, 2663 (1996).
[23] S. Torquato and G. Stell, J. Chem. Phys. **77**, 2071 (1982).
[24] A. Koch, C. Raven, P. Spanne, and A. Snigirev, J. Opt. Soc. Am. A **15**, 1940 (1998).
[25] *The Physics of Medical Imaging*, edited by S. Webb (Institute of Physics, Bristol, 1988).
[26] A. H. Compton, Nobel Lecture, 1927 (unpublished).
[27] K. A. Nugent, T. E. Gureyev, D. F. Cookson, D. Paganin, and Z. Barnea, Phys. Rev. Lett. **77**, 2961 (1996); S. Di Fonzo, W. Jark, G. Soullie, A. Cedola, S. Lagomarsino, P. Cloetens, and C. Riekel, J. Synchrotron Radiat. **5**, 376 (1998).
[28] F. Beckmann, K. Heise, B. Kolsch, U. Bonse, M. F. Rajewsky, M. Bartscher, and T. Biermann, Biophys. J. **76**, 98 (1999); T. E. Gureyev, C. Raven, A. Snigirev, I. Snigireva, and S. W. Wilkins, J. Phys. D **32**, 563 (1999); A. Momose, T. Takeda, Y. Itai, A. Yoneyama, and K. Hirano, J. Synchrotron Radiat. **5**, 309 (1998).
[29] K. H. Kim, Rev. Sci. Instrum. (to be published).
[30] P.-E. Danielsson and O. Seger, in *Machine Vision for Three-Dimensional Scenes*, edited by H. Freeman (Academic, New York, 1990), p. 347.
[31] G. Martinez and G. T. Seidler (unpublished). Complete information on the Hough circle transform can be found in Ref. [33].
[32] P. V. C. Hough, U.S. Patent No. 3069654 (1962).
[33] E. R. Davies, *Machine Vision: Theory, Algorithms, Practicalities* (Academic, New York, 1997), 2nd ed.
[34] L. J. Atkins, G. Martinez, L. H. Seeley, and G. T. Seidler (unpublished).
[35] See, for example, R. Collins, in *Phase Transitions and Critical Phenomena*, edited by C. Domb and M. S. Green (Academic, New York, 1972), Vol. 2.
[36] C. H. Liu, S. R. Nagel, D. A. Schecter, S. N. Coppersmith, S. Majumdar, O. Narayan, and T. A. Witten, Science **269**, 513 (1995); L. Vanel, Ph. Claudin, J.-Ph. Bouchard, M. E. Cates, E. Clement, and J. P. Wittmer, Phys. Rev. Lett. **84**, 1439 (2000).
[37] J. B. Knight, E. E. Ehrichs, V. Y. Kuperman, J. K. Flint, H. M. Jaeger, and S. R. Nagel, Phys. Rev. E **54**, 5726 (1996); D. Howell, R. P. Behringer, and C. Veje, Phys. Rev. Lett. **82**, 5241 (1999); J. A. Astrom, H. J. Herrmann, and J. Timonen, *ibid.* **84**, 638 (2000).
[38] P. M. Chaikin and T. C. Lubensky, *Principles of Condensed Matter Physics* (Cambridge, England, 1995).
[39] X-ray microtomography of granular beds is certainly possible at bending magnet beamlines, but the decreased intensity will require a much larger granule size, thus restricting the vertical height (in units of D) of the sample in the 2-mm high beam; D. M. Mueth, G. F. Debregeas, G. S. Karczmar, P. J. Eng, S. R. Nagel, and H. M. Jaeger, Nature (London) **406**, 385 (2000). Also see O. G. Duliu, Earth-Sci. Rev. **48**, 265 (1999), and references therein for applications of x-ray tomography to the geosciences.
[40] One may speculate about additional technological improvements relevant to data collection rate. For example, projected improvements in frame transfer rates using the IEEE1394 interface in addition to the use of a multilayer monochromator (bandwidth of 50 eV) would together yield at least an order of magnitude improvement in data collection rates before reaching a data mass storage bottleneck; D. Mancini (private communication).